nature sustainability

Article

https://doi.org/10.1038/s41893-023-01071-2

Achieving sustainability of greenhouses by integrating stable semi-transparent organic photovoltaics

Received: 23 February 2022

Accepted: 20 January 2023

Published online: 06 March 2023

Check for updates

Yepin Zhao[1,2,10], Zongqi Li[1,2,10], Caner Deger[3,4,10], Minhuan Wang[5] ✉, Miroslav Peric[6], Yanfeng Yin[5], Dong Meng[1,2], Wenxin Yang[1,2], Xinyao Wang[1,2], Qiyu Xing[1,2], Bin Chang[1,2,7], Elizabeth G. Scott[1,2,8], Yifan Zhou[1,2], Elizabeth Zhang[1,2], Ran Zheng[1,2], Jiming Bian[5], Yantao Shi[9], Ilhan Yavuz[3] ✉, Kung-Hwa Wei[7], K. N. Houk[4] & Yang Yang[1,2] ✉

Semi-transparent organic photovoltaics (OPVs) are an emerging solar-energy-harvesting technology with promising applications, such as rooftop energy supplies for environmentally friendly greenhouses. However, the poor operational stability of OPVs poses challenges to their feasibility as incessantly serving facilities. Here we report a reductive interlayer structure for semi-transparent OPVs that improves the operational stability of OPVs under continuous solar radiation. The interlayer effectively suppresses the generation of radicals from the electron transport layer under sunlight and prevents the structural decomposition of the organic photoactive layer during operation. The defects that serve as the charge carrier recombination sites are nullified by the electron-donating functional groups of the reduced molecules, which improves photovoltaic performance. The semi-transparent OPVs demonstrate a power conversion efficiency of 13.5% and an average visible transmittance of 21.5%, with remarkable operational stability (84.8% retention after 1,008 h) under continuous illumination. Greenhouse results show that the semi-transparent OPV roof benefits the survival rate and growth of the crops, indicating the importance of our approach in addressing food and energy challenges.

Food and energy crises have swept across most of the developing regions around the world in recent decades. Sustainable techniques that efficiently utilize farmland are the key to resolving this problem[1]. Greenhouses, in particular, can effectively prolong the cultivation season by compensating the fluctuating influences of weather and/or temperature over crops and vegetables. Thus, greenhouses have been widely regarded as an effective strategy to boost food yields for the growing human population. However, power grid construction and

[1]Department of Materials Science and Engineering, University of California Los Angeles, Los Angeles, CA, USA. [2]California NanoSystems Institute, University of California Los Angeles, Los Angeles, CA, USA. [3]Department of Physics, Marmara University, Istanbul, Turkey. [4]Department of Chemistry and Biochemistry, University of California Los Angeles, Los Angeles, CA, USA. [5]Key Laboratory of Materials Modification by Laser, Ion, and Electron Beams (Ministry of Education), School of Physics, Dalian University of Technology, Dalian, China. [6]Department of Physics and Astronomy and The Center for Biological Physics, California State University at Northridge, Northridge, CA, USA. [7]Department of Materials Science and Engineering, National Yang Ming Chiao Tung University, Hsinchu, Taiwan. [8]Department of Electrical Engineering, Columbia University, New York, NY, USA. [9]Key Laboratory of Fine Chemicals, Department of Chemistry, School of Chemical Engineering, Dalian University of Technology, Dalian, China. [10]These authors contributed equally: Yepin Zhao, Zongqi Li, Caner Deger. ✉e-mail: wmhkjt@dlut.edu.cn; ilhan.yavuz@marmara.edu.tr; yangy@ucla.edu

electricity consumption used for controlling the inner environment of greenhouses drastically raise the cost, especially in vast remote regions. Hence, a smart greenhouse with semi-transparent organic photovoltaics (OPVs) integrated into the power-generating roof is highly desirable for modern agriculture[2,3].

Due to the unique band structure of organic materials, OPVs are able to selectively absorb light with a desired wavelength[4–6]. Both the power conversion efficiency (PCE) and the average visible transmittance (AVT) of semi-transparent OPVs have improved substantially in recent years[7–12]. The light weight, low cost and flexibility of semi-transparent OPVs further guarantee the promising future of their agricultural application[12–14]. However, the unfavourable functional stability of OPVs seems to be the main issue that hinders the widespread use of semi-transparent OPV-integrated power-generating roofs[15–18]. One of the major origins of OPV instability is photodegradation of the organic molecules due to the superoxide radicals generated from the zinc oxide (ZnO) electron transport layer and their correlated diffusion into the organic photoactive layer[19–21]. The ZnO layer can catalyse the production of superoxide molecules under sunlight, which attack the reductive organic photoactive layer and break down the chemical structure of the organic molecules[22,23]. In addition to this, the electron-trapping defects in the ZnO layer usually serve as the charge carrier recombination site and undermine the photovoltaic performance of the solar cells[24–26]. Thus, an interlayer strategy that can effectively prevent direct contact between the electron transport layer and the photoactive layer without impeding the charge transfer is of particular interest.

Here we report a reductive interlayer based on reduced L-glutathione (L-G; Fig. 1a,b) for our semi-transparent OPV device. The device uses PM6/Y6 (Methods) as the photoactive layer (the structures of PM6 and Y6 molecules are shown in Supplementary Fig. 1). Lower interface resistance and facilitated charge transfer between the ZnO layer and the PM6/Y6 photoactive layer are realized by the insertion of the interlayer. The PCE of the semi-transparent device increases from 11.6% to 13.5%, with an enhancement of the short-circuit current density (J_{sc}) from 20.5 to 22.2 mA cm^{-2}. Additionally, due to the strong reducibility of the L-G molecule, the production of the radicals is reduced. Density functional theory (DFT) based quantum mechanical simulation calculations confirm the defect passivation from the functional groups of the L-G molecules and the superoxide radical suppression effect. After continuous illumination with one-sun intensity for 500 h, the molecular structure and packing in the organic photoactive layer remain almost unchanged, while the reference photoactive layer shows a distinct aggregation and decomposition. The semi-transparent OPVs with the L-G interlayer maintain over 84% of their initial PCE after continuous illumination for 1,008 h. The integration of the resulting semi-transparent OPVs in the power-generating roof shows that plant growth in the semi-transparent OPV-integrated greenhouse is improved relative to that in the traditional glass-roof greenhouse with a higher survival rate. These results reinforce the feasibility of semi-transparent OPVs for agricultural and other relevant applications.

Results

Enhanced photovoltaic performance

As shown in Fig. 1b, the basic device architecture for the semi-transparent OPVs is indium tin oxide (ITO)/ZnO/photoactive layer/MoO_3/ultrathin gold (Au)/ultrathin silver (Ag). In this architecture, the deposition of the ultrathin layer of Au provides nucleation centres that ensure the formation of a continuous thin Ag film. A thin L-G interlayer was inserted between the ZnO layer and the photoactive layer via spin-coating and annealing processes. As confirmed by atomic force microscope images, the morphologies of the ZnO film surface did not change with the incorporation of the L-G layer (Supplementary Fig. 2 and Extended Data Fig. 1). The current density–voltage (J–V) curves of the devices with the interlayer showed an enhancement of J_{sc} (increased from 20.5 mA cm^{-2} to 22.2 mA cm^{-2}, Fig. 1c). As a result, the average PCE of the semi-transparent devices increased from 11.6% to 13.5% (other parameters are summarized in Table 1). The external quantum efficiency (EQE) spectra confirmed the enhanced J_{sc} upon the incorporation of the L-G interlayer (Fig. 1d). The transmittance measurements showed similar AVTs for the devices with and without the L-G interlayer, which indicated that the insertion of the interlayer did not influence the transparency of the semi-transparent solar cells (Fig. 1e). To evaluate the bifacial properties of the semi-transparent devices, we also measured the reflectance and J–V curves of the devices with the interlayer from the Ag side (Supplementary Fig. 3). A PCE of 3.6% with reflectance of 49.1% from 400 nm to 700 nm was obtained (Supplementary Table 1).

We compared the contact resistance of the devices using electrochemical impedance spectroscopy measurements. The OPV devices were biased to the open-circuit potentials. Then they were measured with a low-amplitude a.c. voltage signal. The current densities were measured with different a.c. frequencies to observe the change in the impedance of the devices. The Nyquist plots of the devices (Fig. 1f) were fitted with the equivalent circuit (inset of Fig. 1f). At low frequencies, the impedance response of the semi-transparent solar cell is related to the recombination resistance, R_{rec}, and at high frequencies, the impedance response is related to the charge transfer resistance, R_t. The results showed that the R_{rec} values of the semi-transparent devices with and without the L-G interlayer are similar (the R_{rec} without the L-G interlayer is 10.1 Ω cm^2, while the R_{rec} with the L-G soft interlayer is 10.8 Ω cm^2). In contrast, the R_t reduced from 203.4 Ω cm^2 to 102.5 Ω cm^2 after the incorporation of the L-G interlayer. This result shows that a much lower charge transfer resistance was obtained by inserting the L-G interlayer. Transient photocurrent (TPC) curves of the semi-transparent OPVs were also measured to further compare the charge carrier extraction of the devices with and without the L-G interlayer. The TPC curve of the device with the interlayer shows a faster decay (Fig. 1g), meaning faster charge extraction from the photoactive layer to the electron transport layer. The faster charge extraction indicates less carrier recombination at the interface. It can also explain the higher J_{sc} of the devices with the L-G interlayer from the J–V tests. The facilitated charge transport should be attributed to the lower roughness of the ZnO surface with the L-G interlayer (Extended Data Fig. 1, from 4.6 nm to 3.3 nm). We also measured the photocurrent density (J_{ph}) versus the effective voltage (V_{eff}) of the devices (Fig. 1h), where J_{ph} is the difference between the current densities under illumination and in the dark and V_{eff} is the difference between the voltage when $J_{ph} = 0$ and the applied voltage. All excitons are dissociated into free charge carriers and collected by electrodes at high V_{eff}. In this situation, the saturation photocurrent density (J_{sat}) is only limited by the number of absorbed incident photons. As shown in Fig. 1h, a higher J_{ph}/J_{sat} at low electric field can be obtained by the semi-transparent device with the L-G interlayer than the reference device. It suggests facilitated charge transfer at the interface between the photoactive layer and the electron transport layer with the L-G interlayer.

Simulations

DFT calculations were carried out to understand the physical mechanism underlying the defect passivation effect of the L-G interlayer. The computational details and calculation parameters can be found in the Methods. We first calculated the defect formation energy (DFE) of the wurtzite ZnO surface and identified the two major defects that are easy to form in the ZnO film; that is, oxygen vacancy defects (DFE 0.27 eV) and zinc interstitial defects (DFE 1.05 eV) (Fig. 2a,b). The L-G molecule consists of three parts: glutamate, cysteine and glycine (Fig. 2c). We separately simulated the interaction energy of each part with the two defects. Cysteine was found to have a strong interaction with the oxygen vacancy (interaction energy −4.98 eV) while the glycine interacts tightly with the zinc interstitial (interaction energy −5.46 eV)

https://doi.org/10.1038/s41893-023-01071-2

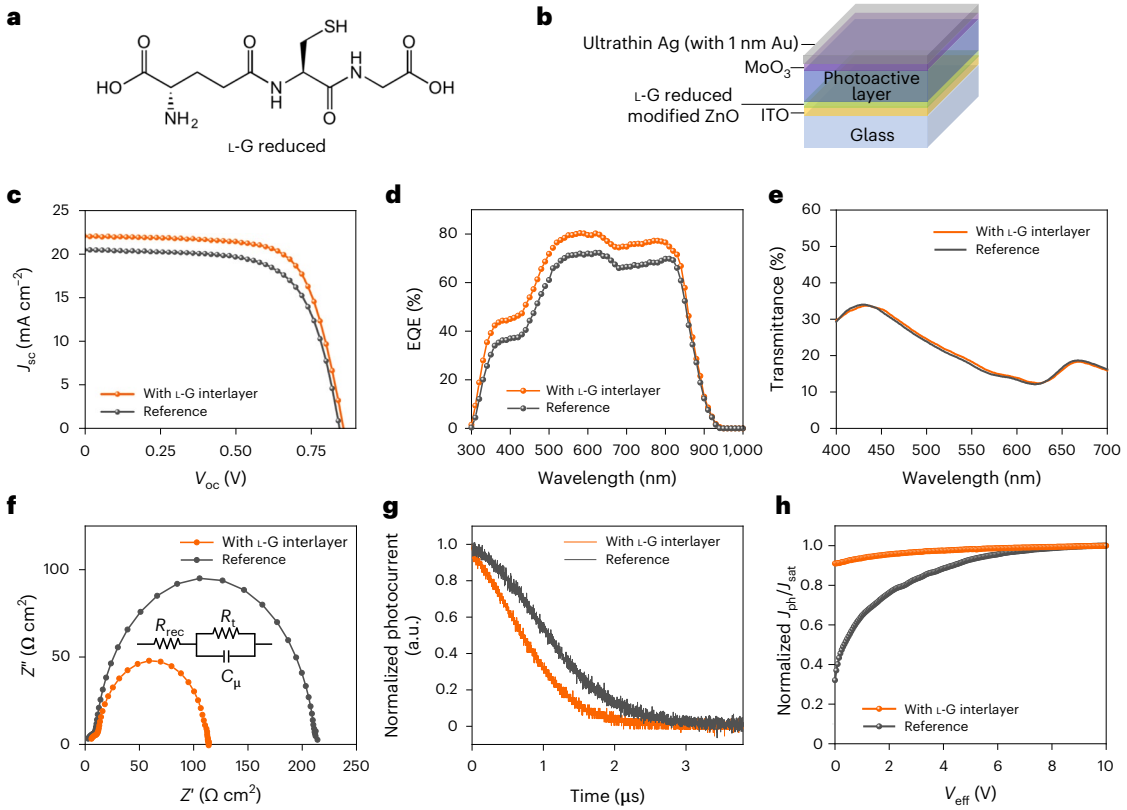

Fig. 1 | Facilitated charge extraction and enhanced photovoltaic performance with the incorporation of the L-G interlayer. a, Molecular structure of reduced L-G. **b**, Device architecture of semi-transparent OPVs with the L-G interlayer. **c**, *J*–*V* curves. **d**, EQE spectra. **e**, Transmittance measurements of the devices with and without the L-G interlayer. **f**, Nyquist plots. The inset shows the equivalent circuit. R_{rec}, recombination resistance; R_t, charge transfer resistance; Z', real part of the impedance; Z'', imaginary part of the impedance; C_μ, chemical capacitance. **g**, TPC curves (a.u., arbitrary units). **h**, Photocurrent data as a function of the effective voltage V_{eff} (potential difference $V_0 - V$) of the devices with and without the L-G interlayer. V_0, voltage when $J_{ph} = 0$; V, applied voltage.

Table 1 | Averages and standard deviations of photoelectric performance and stability under continuous one-sun illumination of semi-transparent OPVs based on PM6/Y6 with and without the L-G interlayer

Device configuration (with PM6/Y6 as active layer)	V_{oc} (V)	J_{sc} (mA cm^{-2})	Fill factor (%)	PCE (%)	AVT (%)	PCE retention after 1,008 h (%)
Semi-transparent OPVs without L-G interlayer	0.84±0.01	20.5±0.2	67.2±0.3	11.6±0.4	21.2±0.3	18.4±6.0
Semi-transparent OPVs with L-G interlayer	0.86±0.01	22.2±0.3	70.4±0.4	13.5±0.4	21.5±0.3	84.8±3.7

V_{oc}, open-circuit voltage.

(Fig. 2d–f). This indicates that the L-G molecule can effectively nullify both major defects in the ZnO film and reduce the carrier recombination at the interface. The passivation effect of the L-G interlayer is also confirmed by the enhanced internal quantum efficiency of the semi-transparent device with the L-G interlayer compared with the internal quantum efficiency of the opaque device without the L-G interlayer (Supplementary Fig. 4). We also investigated the influence of L-G on superoxide formation. There is almost no interaction between the oxygen molecule and the perfect ZnO surface (Supplementary Fig. 5a). However, the oxygen vacancy on the ZnO surface can interact with the oxygen molecule, causing a charge transfer from the surface to the oxygen molecule thus the superoxide formation (Supplementary Fig. 5b,c). In the presence of the L-G molecule, oxygen is not attracted by the oxygen vacancy since the defect is already nullified by the cysteine part of the L-G molecule (Supplementary Fig. 6d). The charge transfer from the ZnO surface to the O_2 is impeded by the L-G molecule, preventing the formation of the superoxide molecule (Supplementary Fig. 5e). Thus, from these simulation results, two different functions of the L-G interlayer can be identified. The first is the defect passivation effect of the L-G interlayer on the ZnO layer. The strong interactions between the L-G molecule and the charge defects on the ZnO surface (that is, oxygen vacancy and zinc interstitial) can alleviate the charge carrier trapping ability of the defects. The second is superoxide suppression, as superoxide formation is usually triggered by the oxygen vacancy on the ZnO surface.

Improved operational stability

To assess morphological changes in the photoactive layer under continuous solar radiation, we compared the grazing-incidence wide-angle X-ray scattering (GIWAXS) patterns of the PM6/Y6 films on ZnO films with and without the L-G interlayer. As shown in Fig. 3a, the 2D GIWAXS patterns are similar before continuous radiation. The diffraction peak

https://doi.org/10.1038/s41893-023-01071-2

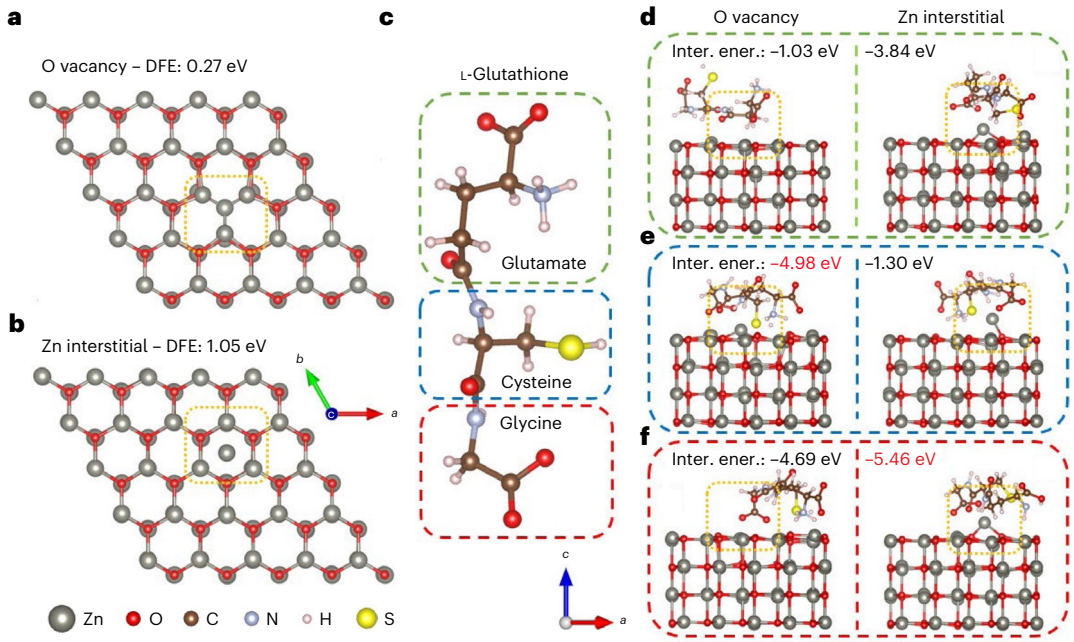

Fig. 2 | Interactions between the L-G molecule and the defects on the ZnO surface. a,**b**, Oxygen vacancy (**a**) and zinc interstitial (**b**) defects (yellow outlines) on the ZnO surface. **c**, The three parts of L-G: glutamate, cysteine and glycine. **d**–**f**, Interaction energies of oxygen vacancy (left) and zinc interstitial (right) defects (yellow outlines) with the glutamate (**d**), cysteine (**e**) and glycine (**f**) parts of L-G. The largest interaction energies (inter. ener.) between oxygen vacancy and zinc interstitial defects and the parts are marked in red.

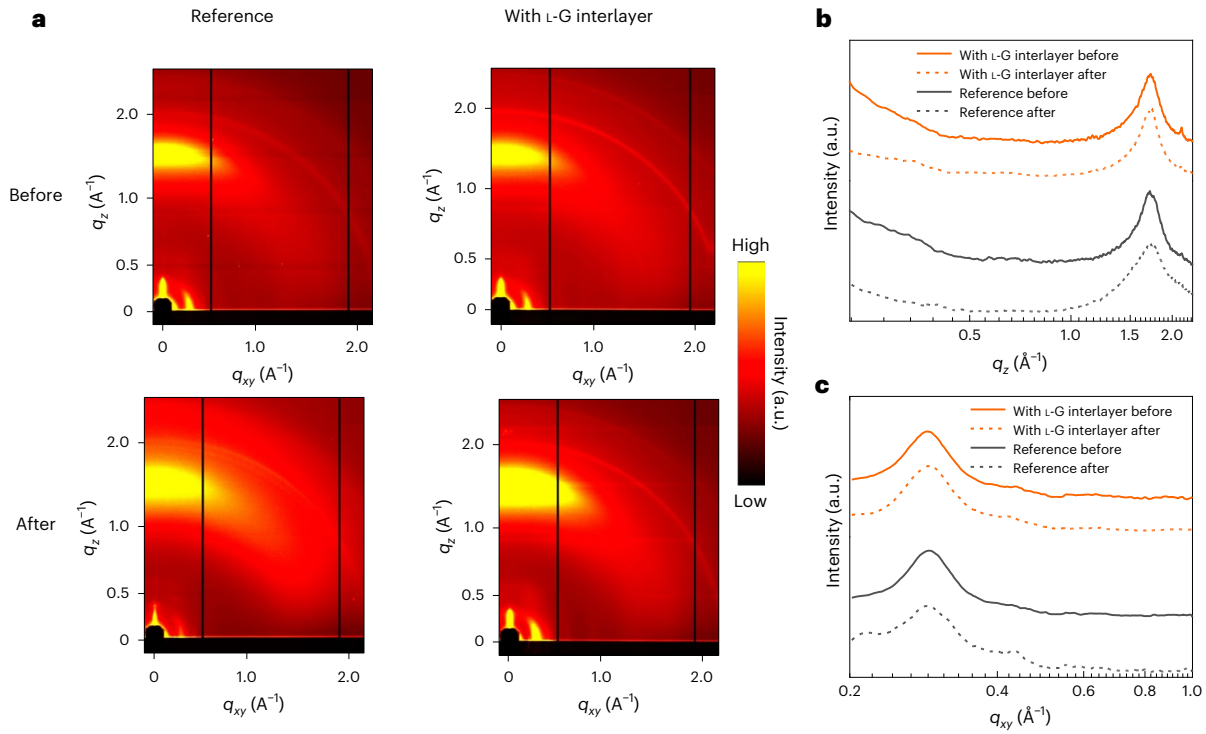

Fig. 3 | Morphological stability of the photoactive layer on the L-G interlayer. a, 2D GIWAXS patterns of the PM6/Y6 films on ZnO films without (reference) and with the L-G interlayer before and after illumination under one-sun intensity for 500 h. **b**,**c**, Corresponding 1D GIWAXS profiles in the out-of-plane (q_z) (**b**) and in-plane (q_{xy}) (**c**) directions (incident angle 0.13°).

at charge state $q = 1.73$ Å^{-1} along the profiles in the out-of-plane direction was assigned to the π–π stacking of PM6, the diffraction peak at $q = 0.29$ Å^{-1} along the in-plane direction was assigned to the lamellar stacking of either Y6 or PM6. Following 500 h of continuous radiation under one-sun intensity in the air, the π–π stacking peak of the organic film on the ZnO layer with the L-G interlayer did not change along the

https://doi.org/10.1038/s41893-023-01071-2

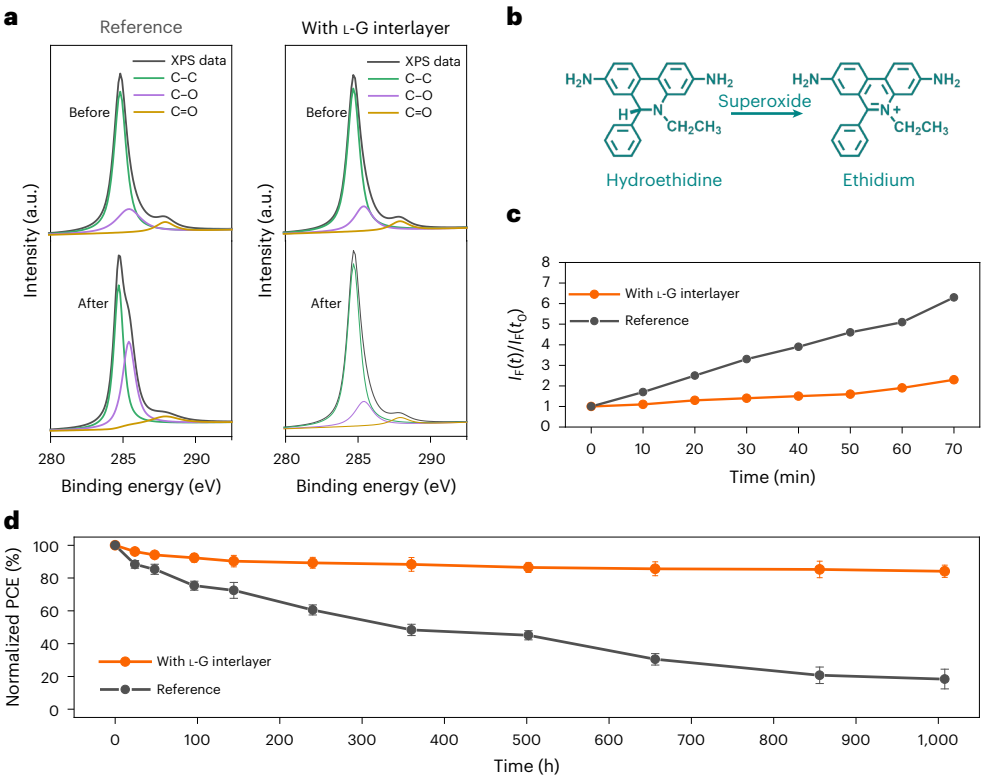

Fig. 4 | Impedance of the organic molecule oxidation by the L-G interlayer and enhanced device stability. a, C 1*s* XPS spectra of the photoactive layer films without (reference) and with the L-G interlayer before and after 300 h of continuous radiation. **b**, Hydroethidine reacts with superoxide radicals to form ethidium. **c**, Normalized fluorescence intensity of the hydroethidine probe as a function of illumination time under AM1.5 G illumination conditions. $I_F(t)$ is the fluorescence maximum at time t and $I_F(t_0)$ is the background fluorescence intensity. $I_F(t)/I_F(t_0)$ corresponds to the yield of superoxide generation. **d**, PCE changes of the devices with and without the L-G interlayer during 1,008 h of exposure under continuous illumination.

out-of-plane direction (Fig. 3b). In contrast, a distinct peak broadening of π–π stacking of the film directly deposited on the ZnO layer indicates decomposition of organic molecules and morphological alteration of the photoactive layer after the continuous radiation. The one-dimensional profile of the film on the ZnO layer without the L-G interlayer along the in-plane direction also showed a broadened peak at $q = 0.29$ Å^{-1} after continuous radiation, suggesting the breakdown of the lamellar structure (Fig. 3c). An additional peak at $q = 0.43$ Å^{-1} was observed in the in-plane direction of the reference sample after continuous radiation in air. This peak should be attributed to the lamellar packing of the Y6 molecules, and it did not appear in the sample with the L-G interlayer. This indicates that the phase separation was suppressed by the interaction between the photoactive layer and the L-G interlayer (Supplementary Fig. 6). The GIWAXS patterns prove that the incorporation of the L-G interlayer can both suppress the degradation of the photoactive layer and reduce molecular aggregation under continuous radiation. We proceeded to compare the C 1*s* X-ray photoelectron spectroscopy (XPS) spectra of the photoactive layer films with and without the L-G interlayer before and after 300 h of continuous radiation (Fig. 4a). The reference film without the interlayer showed a distinct C–O shoulder peak after the exposure, while the spectra of the film with the interlayer remained roughly the same. It experimentally proves that the reductive interlayer successfully impeded the oxidation of the organic molecules in the photoactive layer. The electron paramagnetic resonance (EPR) spectra (Extended Data Fig. 2) show that the superoxide radical signal was greatly reduced under UV radiation with the L-G interlayer. This result manifested the suppression of the superoxide of the L-G molecule, which agrees with the simulation data. To detect the superoxide level inside the photoactive layer, we used hydroethidine as the radical trap (HE probe), which can easily react with the superoxide radicals and transform into ethidium with different photoluminescence peak positions (Fig. 4b). The superoxide generation rate in the organic photoactive layer rate is distinctly slower with the interlayer, once again confirming the superoxide suppression effect. We used coumarin (a compound that specifically reacts with hydroxide radical and produces strong luminescence) to investigate the generation rate of the hydroxide radicals of the ZnO films with and without the L-G interlayer. The results also showed that the hydroxide radicals were largely suppressed by the L-G interlayer (Extended Data Fig. 3). The suppressed superoxide and hydroxide radical generation notably led to enhanced operational stability of the encapsulated semi-transparent OPV devices with the PM6/Y6 photoactive layer (Fig. 4c). The devices with the L-G interlayer retained over 84% of their initial efficiency after 1,008 h continuous exposure under illumination. The tests were implemented under a metal-halogen xenon lamp source (90 ± 10 mW cm^{-2}) at a temperature of around 45 °C and with a relative humidity of about 40% (Fig. 4d). To reduce the influence of morphological change and enhance the light-induced oxidation effect, we tested the unencapsulated devices under 5-sun illumination at a temperature of 45 °C and a relative humidity of about 40%. The results show that the devices with the L-G interlayer maintained about 63% of their initial PCEs while the reference devices completely degraded after 502 h (Extended Data Fig. 4a). We also tested the thermal stability of semi-transparent devices with and without the L-G interlayer in an inert environment. The ones with the interlayer maintained over 70% of their initial PCEs while the reference devices lost about 95% of their initial PCEs after 502 h (Extended Data Fig. 4b). This should be attributed to the interactions between the L-G interlayer and the photoactive layer

https://doi.org/10.1038/s41893-023-01071-2

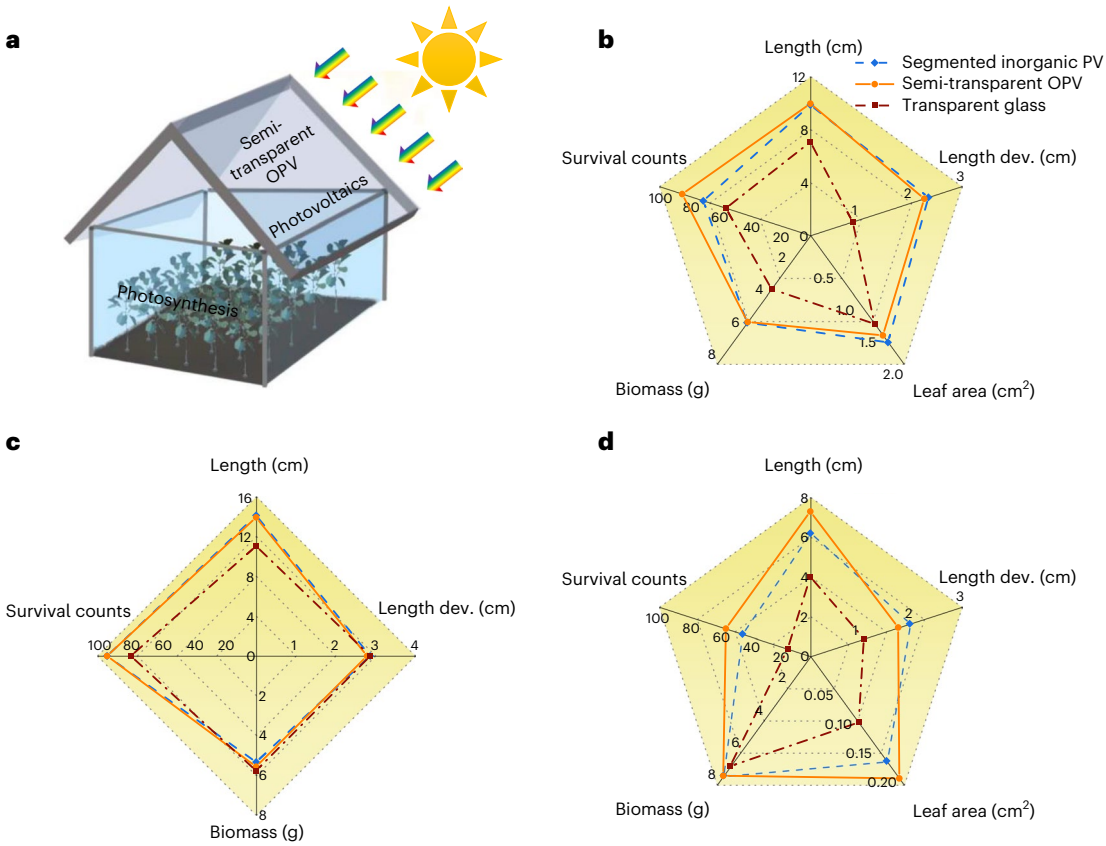

Fig. 5 | Plant growth in the integrated photovoltaics/photosynthesis system. **a**, Schematic of the power-generating greenhouse with semi-transparent OPV roof. **b**–**d**, Plant growth metrics for mung bean (**b**), wheat (**c**) and broccoli (**d**). Biomass among different plants is normalized into the final mass with 1 g initial seed mass. The survival count is normalized by the number of survived plants per 100 initial seeds. The legend in **b** also applies to **c** and **d**. Length dev. means the length standard deviation of the plants.

molecules. The interactions alleviated molecule aggregation and phase separation of the photoactive layer during the stability tests. This is also confirmed by the morphology changes of the photoactive layers on ZnO layer with and without L-G interlayer (Extended Data Fig. 5).

Plant growth metrics

To verify the potential to grow various plants in the photovoltaics/photosynthesis integrated system, we built greenhouses with the semi-transparent OPV roofs incorporating the L-G interlayer and compared the growth conditions of multiple common crops (that is, mung bean, wheat and broccoli sprout) in those greenhouses with crops growing in greenhouses with roofs of transparent glass and segmented inorganic solar cells (Fig. 5a and Supplementary Figs. 7 and 8). We monitored the growing conditions of the plants for 8 consecutive days under natural sunlight without a UV filter (Extended Data Figs. 6–8). As shown in Fig. 5b–d, we summarized the sprout lengths, length deviations, biomass productivities and survival rates of the plants after 8 days of growth as the parameters of the evaluation. Since the wheat sprouts do not have leaves, we only included the leaf area data for the mung bean and broccoli. Both the sprout lengths and survival rates of the plants grown in the greenhouses with semi-transparent OPV roofs are comparable to or higher than the plants grown in the greenhouses with transparent glass or spatially segmented inorganic solar-cell roofs. The higher survival rates should be attributed to the UV-light-absorbing properties of the roofs that were fully covered with semi-transparent OPVs as the UV exposure undermines the biological activity of the sprouts[27–29]. To confirm this, we also integrated a UV filter over the greenhouses during another batch of plant growth. As shown in Supplementary Fig. 9, the height, number of the branches and the leaf area of the sprouts grown under the transparent glass roof were comparable to (or slightly higher than) those of the plants grown in the greenhouse with the semi-transparent OPV roof. The results indicate that the integration of the semi-transparent OPVs in greenhouse roofs will not impair the growth of the plants (by competing for the sunlight absorption). Interestingly, the semi-transparent OPV roof could protect the plants from detrimental UV exposure and promote the growth of the plants in the greenhouses. In this case, the photovoltaic and photosynthetic systems can benefit each other by the integration. The biomass productivity together with the concurrent electricity production of the system are estimated in Supplementary Table 2. Combined with the extended operational lifetime of the semi-transparent OPVs with the L-G interlayer, successful commercialization of environmentally friendly greenhouses can be expected.

Discussion

As photovoltaics and photosynthesis serve as two major strategies to acquire sustainable energy directly from the Sun, the integration of semi-transparent OPVs into power-generating roofs of greenhouses could greatly increase the utilization of sunlight. To realize the successful integration of the two renewable power-generating systems, the stability of solar-cell devices and the benificial effects of solar cells on greenhouse planting play important roles. Aiming to resolve the stability issue of semi-transparent OPVs, we introduced a reductive interlayer into the device architecture. Charge carrier extraction and transportation were enhanced due to the nullification of the charged

charger traps in the ZnO layer. The insertion of the L-G interlayer led to an improved average PCE of 13.5% while maintaining the AVT of the semi-transparent devices. Suppressed superoxide generation was observed under radiation. As a result, the PCE of the devices with the L-G interlayer remained over 84% after continuous illumination for 1,008 h. Greenhouse roofs with semi-transparent OPV devices have the potential to deliver healthy growth of various plants with higher survival rates. The roof with semi-transparent OPVs protected the plants from harmful sunlight, unlike the roofs with transparent glass or segmented opaque inorganic solar cells. Our study highlights the importance of the operational stability of OPVs and the reciprocity between photovoltaic and photosynthetic systems through the integration of the semi-transparent OPVs as the greenhouse roof. The integrated system could be very beneficial when applied on a larger scale and may contribute to addressing food and energy challenges in densely populated areas without extra pollution or land usage.

Methods

Materials

All chemicals were obtained from commercial suppliers and used without further purification. The polymer donor PM6 (poly[(2,6-(4,8-bis(5-(2-ethylhexyl-3-fluoro)thiophen-2-yl)-benzo[1,2-*b*:4,5-*b*′]dithiophene))-alt-(5,5-(1′,3′-di-2-thienyl-5′,7′-bis(2-ethylhexyl) benzo[1′,2′-*c*:4′,5′-*c*′]dithiophene-4,8-dione)]) and acceptor Y6 (2,20-((2Z,20Z)-((12,13-bis(2-ethylhexyl)-3,9-diundecyl-12,13-dihydro-[1,2,5]thiadiazolo[3,4-e]thieno[2,′30′:4′,50] thieno[20,30:4,5] pyrrolo[3,2-g]thieno[20,30:4,5]thieno[3,2-*b*]indole-2,10-diyl) bis(methanylylidene)) bis(5,6-difluoro-3-oxo-2,3-dihydro-1H-indene-2,1-diylidene))dimalononitrile) were purchased from Solarmer, Inc. Chloroform and 1-chloronaphthalene were obtained from Sigma-Aldrich, Inc. For the interlayer, L-G and pure water were purchased from Sigma-Aldrich, Inc. For the transport layers, ZnO nanoparticle solution and MoO_3 powder were also purchased from Sigma-Aldrich, Inc. Coumarin was purchased from Alfa Aesar Co., Ltd.

Solar cell fabrication

Organic solar cells were made with the following structure: ITO/ZnO/photoactive layer/MoO_3/Ag (various thicknesses). The ITO glass substrates were pre-cleaned in an ultrasonic bath of acetone and isopropanol and then dried with nitrogen. Before coating with the ZnO layer, the substrates were treated in an ultraviolet-ozone chamber (Jelight Company) for 10 min. A thin layer (about 30 nm) of ZnO sol-gel was spin-coated onto the ITO substrate surface, and then the substrates were baked at 200 °C for 60 min. The L-G interlayer was applied by spin-coating a solution with L-G dissolved in pure water (1.5 mg ml^{-1}) onto the ZnO layer. The solution (20 µl) was dripped onto the ZnO layer surface after the substrate reached and was kept at 4,000 r.p.m. The spinning was stopped after 10 s and the substrate was immediately moved and baked at 95 °C for 3 min in the nitrogen glovebox. To obtain the photoactive layers, a mixture of PM6/Y6 (7:9, by weight) was dissolved in a chloronaphthalene/chloroform (0.5%, by volume) solvent. Then the solution was stirred for 1.5 h (60 °C) before use. To form the photoactive layers, the blended solutions were spin-coated on the ZnO layer. The thickness of the photoactive layer was 90–110 nm. A MoO_3 (about 10 nm) and Ag layer (100 nm for opaque OPVs; 15 nm for semi-transparent OPVs) was then evaporated onto the surface of the photosensitive layer under vacuum (approximately 10^{-5} Pa) as the electrodes. The active area of the device was 0.12 cm^2. For semi-transparent OPVs, a 1 nm Au layer was evaporated before the deposition of Ag. The device encapsulation was conducted in a nitrogen atmosphere. We covered the glass slits with the UV curable sealant (Norland Optical Adhesives 60) and put them on the metal electrode side of the organic devices. A UV lamp (UVP Analytik Jena) was used for adhesive curing for 10 s at a distance of about 3 cm with an intensity of about 5 mW cm^{-2}.

Device characterization

The *J*–*V* curves of the solar cells were measured with a Keithley 2401 source meter, under simulated one-sun illumination (AM 1.5 G, 100 mW cm^{-2}) (Oriel Sol3A with class AAA solar simulator, Newport). The intensity calibration of the light was carried out by using an NREL-certified Si photodiode with a KG-5 filter. Solar cell measurements were performed in an ambient atmosphere without pre-conditioning such as voltage bias or light soaking. A scan rate of 0.1 V s^{-1} (−1.0 V to 1.0 V) was used for *J*–*V* characterizations with a mask with an area of 0.1 cm^2.

The EQE measurements were carried out by a specially designed system (Enli tech). The system operated in a.c. mode (chopping frequency: 133 Hz) without bias light. All optical and mechanical components were integrated inside the 60 cm × 60 cm × 60 cm main body with electrical signal acquisition lock-in amplifiers. The lamp wavelength range was from 250 nm to 2500 nm (Xe75). A Si diode (RC-S103011) was used for calibration before the measurements. The devices were measured in the dark using a 3M clip (923690-14). Electrochemical impedance spectroscopy was performed with an electrochemical workstation (Zennium Zahner) with a 20 mV amplitude for a.c. perturbations ranging from 100 mHz to 1 MHz. The transmittance spectra of the semi-transparent OPVs were obtained using a U-4100 spectrophotometer (Hitachi) equipped with integrating sphere. During the measurements, the monochromatic light was incident on the substrate side. The TPC measurements were carried out with a white light bias. The bias was generated from an array of diodes (Molex 180081-4320) to simulate 0.5-sun bias light working conditions. The perturbation source was a pulsed laser (510 nm) pumped by a nitrogen laser (LSI VSL-337ND-S). The pulse width was 3 ns, and the repetition frequency was 3 Hz. To ensure that the perturbation assumption of excitation light held, the intensity of the perturbation laser pulse was controlled to maintain the amplitude of transient V_{oc} below 5 mV. The currents under short-circuit conditions were measured over a 50 Ω resistor. The data were recorded on a digital S4 oscilloscope (Tektronix DPO 4104B).

Film characterization

The GIWAXS measurement was performed at the Advanced Light Source on the 7.3.3. beamline. All samples were deposited on the silicon wafer with 100 nm silicon oxide. To obtain the ω:2θ scans (ω is defined as angle between the incident X-ray and out-of-plane crystal axis and 2θ is defined as angle between the incident and scattered X-rays), a high-resolution X-ray diffractometer with Cu Kα radiation was employed. Samples were irradiated by 10 keV at a fixed X-ray incident angle of 0.10–0.14° with an exposure time of 3 s. XPS measurements were carried out on an XPS AXIS Ultra DLD (Kratos Analytical). An Al Kα (1,486.6 eV) X-ray was used as the excitation source. For superoxide probe measurements, we dissolved 10 mg hydroethidine in 10 ml toluene to make 31.7 µM solution of the hydroethidine probe. Sonication was used to facilitate miscibility. We then made 10 ml of 0.317 µM solution by diluting from the stock solution and put the samples inside. The photoluminescence spectra were recorded on a Horiba Yobin-Ybon Fluorolog-3 spectrofluorometer. The excitation wavelength was 520 nm and the slit width was 10 mm. For hydroxide probe measurements, ZnO films with and without L-G interlayer were dispersed in 10 ml of 0.001 M COU aqueous solution in a 7 cm dish. A 350 W Xenon arc lamp (Ushio America, Inc.) was used as a light source. We ensured that the average light intensity on the surface of the solution was about 5.0 mW cm^{-2} by changing the distance between the solution and the lamp. The light intensity was measured by a UV radiometer (Model: Rejuvenate UVoT UV HVAC Monitor System) with a peak intensity of 365 nm. Fluorescence spectra of generated 7-hydroxycoumarin were measured on a Hitachi Fluorolog-3 fluorescence spectrophotometer with an excitation wavelength of 332 nm.

Computational method

All surface calculations for the ZnO layer were performed using plane-wave based DFT. 5 × 5 × 2 ZnO slabs were generated along the wurtzite [001] direction and a 10–15 Å vacuum slab was added. The Perdew–Burke–Ernzerhof-type generalized gradient approximation for the exchange-correlation functional with a 300 eV plane-wave cutoff and 4 × 4 × 1 k-point mesh for Brillouin zone sampling was chosen for all geometry optimizations and self-consistent field calculations[30–32]. Dispersion corrections to electronic energies based on Grimme's DFT-D3(BJ) scheme were included[32]. Ionic positions and volumes were relaxed using a conjugate gradient algorithm, until all residual forces were smaller than 0.01 eV $Å^{-1}$. First-principles calculations were performed based on the DFT using a plane-wave basis set and the projected augmented wave method. It was implemented in the VASP package[33,34].

Defect formation energies were predicted using the following formula:

$$\Delta H_d^q = E_d^q - E_0 + \sum_i \Delta n_i \mu_i$$

where d is the defective energy, E_0 is the non-defective energy, Δn_i is the number change in element removal (or addition) to create the defect and μ_i is the corresponding chemical potential.

Defect-molecule interaction energies were predicted using the expression:

$$E_{\text{int}} = E_{\text{d,m}} - [E_{\text{d}} + \mu_{\text{m}}]$$

where $E_{\text{d,m}}$ is the total energy of the supercell containing the defect plus molecule, E_{d} is the total energy of the system with the defect only and μ_{m} is the chemical potential of the molecule.

The charge density difference was calculated to quantify the charge transfer between the defect and the molecule. It can be calculated using the following formula:

$$\Delta\rho = \rho_{comp} - \rho_{surf} - \rho_{mol}$$

where ρ_{comp}, ρ_{surf} and ρ_{mol} are the charge density distributions of the defective surface-molecule complex, defective surface and free molecule, respectively.

EPR measurements

Electron spin resonance (ESR) measurements were performed on a Bruker EMXPlus ESR spectrometer equipped with a TE011 microwave cavity ER 4119HS. Before the EPR measurements, OPV samples with and without the L-G layer were placed in a 50 mM solution of 5,5-dimethyl-1-pyrroline-N-oxide (DMPO), obtained from Sigma-Aldrich, Inc., in a solution of anhydrous dimethyl sulfoxide, also purchased from Sigma-Aldrich, Inc. Samples were drawn into open-ended polytetrafluoroethylene (PTFE-ID: AWG21) tubing bought from Zeus. The tubing was folded in half, and the open ends were squeezed by pliers. After folding, the tubing was then placed into a quartz tube made by Wilmad Glass Co. The tube was then placed in the ESR cavity. The EPR spectra represent the average of five runs and were acquired employing a sweep time of 10 s, microwave frequency of 9.297431 GHz, microwave power of 6.3 mW, sweep width of 80 G and modulation amplitude of 1 G. After taking an ESR spectrum without UV illumination, the sample was taken out of the cavity and illuminated with a UVG-54 handheld UV lamp (254 nm 6 W) for 5 min. Then, the sample was promptly put in the cavity and measured again. The ESR signal of the DMPO–$O_2^{\bullet-}$ adduct has a characteristic spectrum[35] (Extended Data Fig. 2).

Greenhouse assembly

Transparent plexiglass sheets (Sosco Metals) were used to build greenhouse frameworks with a length of 30 cm, a width of 21.5 cm and a height of 15 cm. Semi-transparent organic solar panels, opaque organic solar panels, segmented inorganic solar panels and transparent panels were studied. Each greenhouse had two roof surfaces with a length of 30 cm and a width of 15 cm angled at 45° towards the horizon. To ensure complete coverage of the solar cells between the lighting and the plant, the walls of each greenhouse were covered by black tape and aluminium foil during plant growth. Rectangular polypropylene trays (SHEING) with a length of 26.5 cm and a width of 19.5 cm were used to germinate the plants and were placed directly under the greenhouses. When verifying the influence of the UV light on plant growth, we added an extra UV filter (Edmund Optics) on the top of the greenhouse roofs.

Measuring plant growth conditions

Three types of commonly consumed plants (mung bean, wheat and broccoli sprout) were chosen to evaluate the growing conditions under greenhouses with different roofs. Given the different sizes of the seeds, seed spacings for mung bean, wheat and broccoli sprouts were 0.2 count cm^{-2}, 0.3 count cm^{-2} and 2.7 count cm^{-2}, respectively. All seeds were immersed in water for 1 day before being placed evenly in trays with water underneath. Then, each tray was loaded with a different greenhouse and placed outside for 8 consecutive days. The water temperature in the greenhouses was kept stable by changing it with fresh water (~20 °C) every hour during the daytime. The environmental conditions of plant growth are summarized in Supplementary Table 3. The height of the plants was monitored daily at 6 p.m., and the water was refilled to ensure that the plants stayed hydrated. The length of the sprouts was measured based on the distance from the top to the beginning of the root. The area of the leaves was measured by taking off the leaves and analysing them using ImageJ (version 1.52a)[36]. The survival rate was calculated by counting the number of surviving sprouts normalized by the number of initial seeds. All the plants in the different greenhouses were counted and averaged for statistical analysis.

Biomass productivity calculation

To evaluate the plant biomass productivity, we measured the biomass of the different crops after growing in the greenhouses for 8 days. We measured the biomass by summing the dry mass of all organics, including the surviving sprout, the roots, dead sprouts and ungerminated seeds. We placed them in a 90 °C oven for 3 days to remove excess water[37]. The weight of each batch was measured using a balance, and the final weight was normalized based on its initial mass for the convenience of comparison. We then calculated the biomass productivity by using the following equation[38–40]:

$$P = (N_2 - N_1)/(t_2 - t_1)$$

where N_1 and N_2 are defined as the biomass at time 1 (t_1) and time 2 (t_2), respectively.

Estimated electricity production

Global horizontal irradiance (GHI) is defined as the total solar radiation incident on a horizontal surface. It is the sum of diffuse horizontal irradiance, direct normal irradiance and ground-reflected radiation. The GHI values used to evaluate the concurrent electricity production were provided by Solcast. The local cloud cover was included to render a precise and accurate local snapshot of solar irradiance. The GHI data were collected at UCLA every 60 min and are summarized in Supplementary Tables 3–5. The total energy power and the daily average power for each round of plant growth were calculated on the basis of the GHI profile. Considering the performance loss during scaling up, we used 20% and 11% as the PCEs for inorganic solar cells and semi-transparent solar cells in the estimation. The electricity production for each greenhouse was calculated on the basis of the roof panel size, the angle to the horizon and the GHI profile.

Data availability

All relevant data that support the findings of this study are presented in the article and Supplementary Information. Source data are available from the corresponding authors upon reasonable request.

References

1. Wu, A., Hammer, G. L., Doherty, A., von Caemmerer, S. & Farquhar, G. D. Quantifying impacts of enhancing photosynthesis on crop yield. *Nat. Plants* **5**, 380–388 (2019).
2. Joshi, S. et al. High resolution global spatiotemporal assessment of rooftop solar photovoltaics potential for renewable electricity generation. *Nat. Commun.* **12**, 5738 (2021).
3. Ballif, C., Perret-Aebi, L.-E., Lufkin, S. & Rey, E. Integrated thinking for photovoltaics in buildings. *Nat. Energy* **3**, 438–442 (2018).
4. Li, G., Zhu, R. & Yang, Y. Polymer solar cells. *Nat. Photon.* **6**, 153–161 (2012).
5. Hou, J., Inganäs, O., Friend, R. H. & Gao, F. Organic solar cells based on non-fullerene acceptors. *Nat. Mater.* **17**, 119–128 (2018).
6. Chang, S.-Y., Cheng, P., Li, G. & Yang, Y. Transparent polymer photovoltaics for solar energy harvesting and beyond. *Joule* **2**, 1039–1054 (2018).
7. Betancur, R. et al. Transparent polymer solar cells employing a layered light-trapping architecture. *Nat. Photon.* **7**, 995–1000 (2013).
8. Traverse, C. J., Pandey, R., Barr, M. C. & Lunt, R. R. Emergence of highly transparent photovoltaics for distributed applications. *Nat. Energy* **2**, 849–860 (2017).
9. Wang, D. et al. High-performance and eco-friendly semitransparent organic solar cells for greenhouse applications. *Joule* **5**, 945–957 (2021).
10. Li, Y. et al. Color-neutral, semitransparent organic photovoltaics for power window applications. *Proc. Natl Acad. Sci. USA* **117**, 21147–21154 (2020).
11. Wang, D. et al. High-performance semitransparent organic solar cells with excellent infrared reflection and see-through functions. *Adv. Mater.* **32**, 2001621 (2020).
12. Li, Y. et al. High efficiency near-infrared and semitransparent non-fullerene acceptor organic photovoltaic cells. *J. Am. Chem. Soc.* **139**, 17114–17119 (2017).
13. Ravishankar, E. et al. Achieving net zero energy greenhouses by integrating semitransparent organic solar cells. *Joule* **4**, 490–506 (2020).
14. Kaltenbrunner, M. et al. Ultrathin and lightweight organic solar cells with high flexibility. *Nat. Commun.* **3**, 770 (2012).
15. Burlingame, Q., Ball, M. & Loo, Y.-L. It's time to focus on organic solar cell stability. *Nat. Energy* **5**, 947–949 (2020).
16. Burlingame, Q. et al. Intrinsically stable organic solar cells under high-intensity illumination. *Nature* **573**, 394–397 (2019).
17. Ghasemi, M. et al. A molecular interaction–diffusion framework for predicting organic solar cell stability. *Nat. Mater.* **20**, 525–532 (2021).
18. Deschler, F. et al. The effect of ageing on exciton dynamics, charge separation, and recombination in P3HT/PCBM photovoltaic blends. *Adv. Funct. Mater.* **22**, 1461–1469 (2012).
19. Jiang, Y. et al. Photocatalytic effect of ZnO on the stability of nonfullerene acceptors and its mitigation by SnO_2 for nonfullerene organic solar cells. *Mater. Horiz.* **6**, 1438–1443 (2019).
20. Li, Y. et al. Non-fullerene acceptor organic photovoltaics with intrinsic operational lifetimes over 30 years. *Nat. Commun.* **12**, 5419 (2021).
21. Duan, L. & Uddin, A. Progress in stability of organic solar cells. *Adv. Sci.* **7**, 1903259 (2020).
22. Hoke, E. T. et al. The role of electron affinity in determining whether fullerenes catalyze or inhibit photooxidation of polymers for solar cells. *Adv. Energy Mater.* **2**, 1351–1357 (2012).
23. Luke, J. et al. Twist and degrade—impact of molecular structure on the photostability of nonfullerene acceptors and their photovoltaic blends. *Adv. Energy Mater.* **9**, 1803755 (2019).
24. Gokulnath, T. et al. A wide-bandgap π-conjugated polymer for high-performance ternary organic solar cells with an efficiency of 17.40%. *Nano Energy* **89**, 106323 (2021).
25. Jiang, H. et al. Passivated metal oxide n-type contacts for efficient and stable organic solar cells. *ACS Appl. Energy Mater.* **3**, 1111–1118 (2019).
26. Palilis, L. C. et al. Inorganic and hybrid interfacial materials for organic and perovskite solar cells. *Adv. Energy Mater.* **10**, 2000910 (2020).
27. Larson, R. A. & Berenbaum, M. R. Environmental phototoxicity. *Environ. Sci. Technol.* **22**, 354–360 (1988).
28. Mackerness, S. A.-H. Plant responses to ultraviolet-B (UV-B: 280–320 nm) stress: what are the key regulators? *Plant Growth Regul.* **32**, 27–39 (2000).
29. Caldwell, M. *Physiological Plant Ecology I* (Springer, 1981).
30. Perdew, J. P., Burke, K. & Ernzerhof, M. Generalized gradient approximation made simple. *Phys. Rev. Lett.* **77**, 3865–3868 (1996).
31. Perdew, J. P. et al. Restoring the density-gradient expansion for exchange in solids and surfaces. *Phys. Rev. Lett.* **100**, 136406 (2008).
32. Grimme, S. Semiempirical GGA-type density functional constructed with a long-range dispersion correction. *J. Comp. Chem.* **27**, 1787–1799 (2006).
33. Kresse, G. & Furthmüller, J. Efficiency of ab-initio total energy calculations for metals and semiconductors using a plane-wave basis set. *Comput. Mater. Sci.* **6**, 15–50 (1996).
34. Kresse, G. & Furthmüller, J. Efficient iterative schemes for ab initio total-energy calculations using a plane-wave basis set. *Phys. Rev. B* **54**, 11169 (1996).
35. Zang, L. Y. & Misra, H. P. EPR kinetic studies of superoxide radicals generated during the autoxidation of 1-methyl-4-phenyl-2,3-dihydropyridinium, a bioactivated intermediate of parkinsonian-inducing neurotoxin 1-methyl-4-phenyl-1,2,3,6-tetrahydropyridine. *J. Biol. Chem.* **267**, 23601–23608 (1992).
36. Schneider, C. A., Rasband, W. S. & Eliceiri, K. W. NIH Image to ImageJ: 25 years of image analysis. *Nat. Methods* **9**, 671–675 (2012).
37. Maldonado, M., Ribes, M. & van Duyl, F. C. Nutrient fluxes through sponges: biology, budgets, and ecological implications. *Adv. Mar. Biol.* **62**, 113–182 (2012).
38. Young, H. E., Schlegel, H. G. & Barnea, J. (eds) *Microbial Energy Conversion* (Pergamon, 1977).
39. Zhu, J. et al. Improved productivity of neutral lipids in *Chlorella* sp. A2 by minimal nitrogen supply. *Front. Microbiol.* **7**, 557 (2016).
40. Pandey, A., Larroche, C. & Ricke, S. C. (eds) *Biofuels: Alternative Feedstocks and Conversion Processes* (Academic, 2011).

Acknowledgements

This work is supported by the California Energy Commission (grant no. EPC-19-002). Computing resources used in this work were provided by the National Center for High Performance Computing (UHeM) of Turkey (grant no. 1008342020). C.D. would like to thank the Fulbright Turkey Commission for providing a valuable scholarship for his post-doctoral study in the United States. M.W. acknowledges financial support from the National Natural Science Foundation of China (NSFC) (grant nos 12104081 and 51872036) and China Postdoctoral Science Foundation (grant no. 2022T150087). M.P. acknowledges financial support from the National Science

Foundation Research in Undergraduate Institutions (RUI) (grant no. 1856746).

Author contributions

Y. Zhao and Y. Yang conceived the idea. Y. Zhao conducted the experiments and prepared the paper under the supervision of Y.Y. C.D. and I.Y. performed the DFT calculations. Z.L. prepared the samples for EQE, GIWAX and XPS measurements. Z.L. collected GIWAX data of the films. M.P. conducted the EPR measurements. Q.X. helped with the XPS measurements. M.W. and Y. Yin collected electrochemical impedance spectroscopy and TPC data under the supervision of Y.S. and J.B. Z.L. and X.W. built the PV-integrated greenhouses and did the correlated plant observation under the sunlight. B.C. and E.G.S. helped with the estimation of biomass productivity and concurrent electricity production under the supervision of K.-H.W. W.Y., Y. Zhou, D.M., E.Z., R.Z., Y.S. and K.N.H. provided helpful discussion during the project and revised the paper. All the authors discussed the results and commented on the paper.

Competing interests

The authors declare no competing interests.

Additional information

Extended data is available for this paper at https://doi.org/10.1038/s41893-023-01071-2.

Supplementary information The online version contains supplementary material available at https://doi.org/10.1038/s41893-023-01071-2.

Correspondence and requests for materials should be addressed to Minhuan Wang, Ilhan Yavuz or Yang Yang.

Peer review information *Nature Sustainability* thanks Chang-Zhi Li, Jianhui Hou and the other, anonymous, reviewer(s) for their contribution to the peer review of this work.

Reprints and permissions information is available at www.nature.com/reprints.

Publisher's note Springer Nature remains neutral with regard to jurisdictional claims in published maps and institutional affiliations.

Springer Nature or its licensor (e.g. a society or other partner) holds exclusive rights to this article under a publishing agreement with the author(s) or other rightsholder(s); author self-archiving of the accepted manuscript version of this article is solely governed by the terms of such publishing agreement and applicable law.

© The Author(s), under exclusive licence to Springer Nature Limited 2023

https://doi.org/10.1038/s41893-023-01071-2

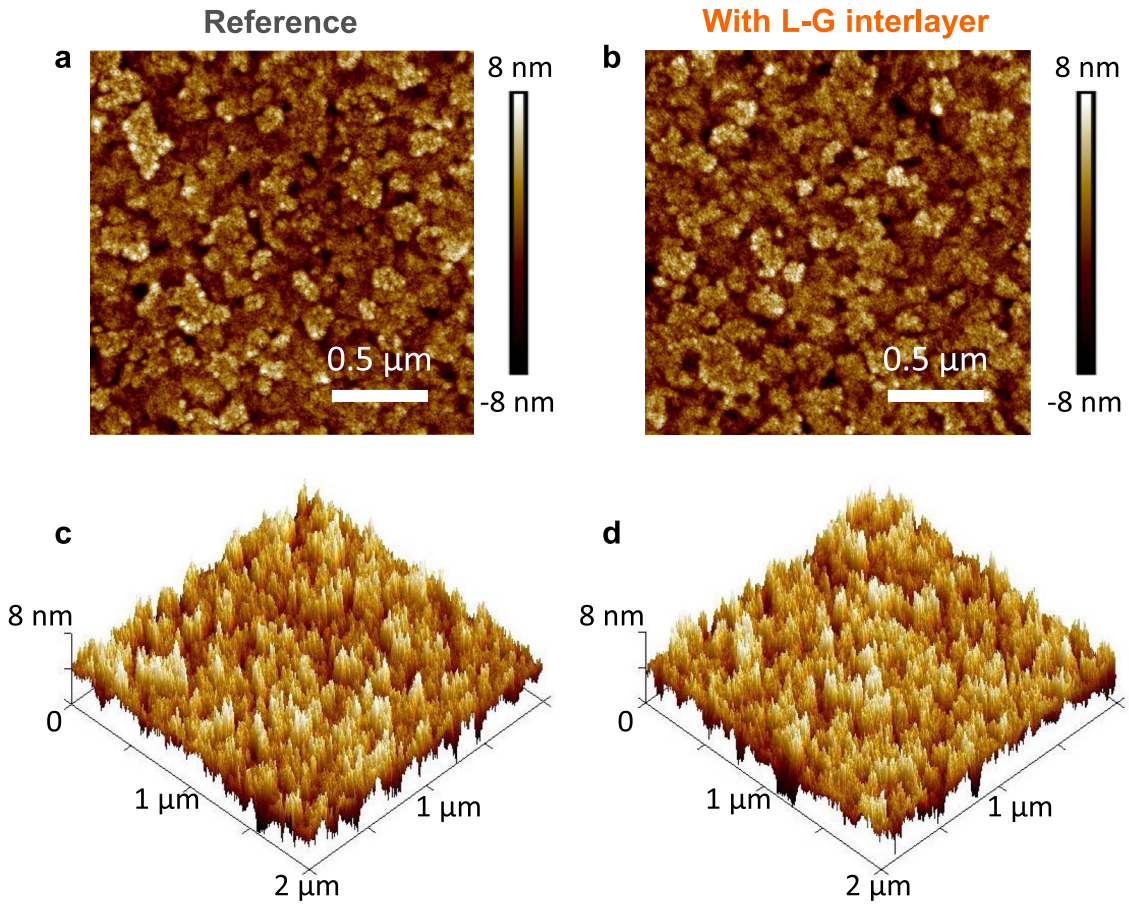

Extended Data Fig. 1 | Surface morphology of the ZnO layer with and without L-G interlayer. AFM images of the ZnO surface a, without and b, with the L-G interlayer, and three-dimensional AFM images of ZnO films c, without and d, with L-G interlayer.

https://doi.org/10.1038/s41893-023-01071-2

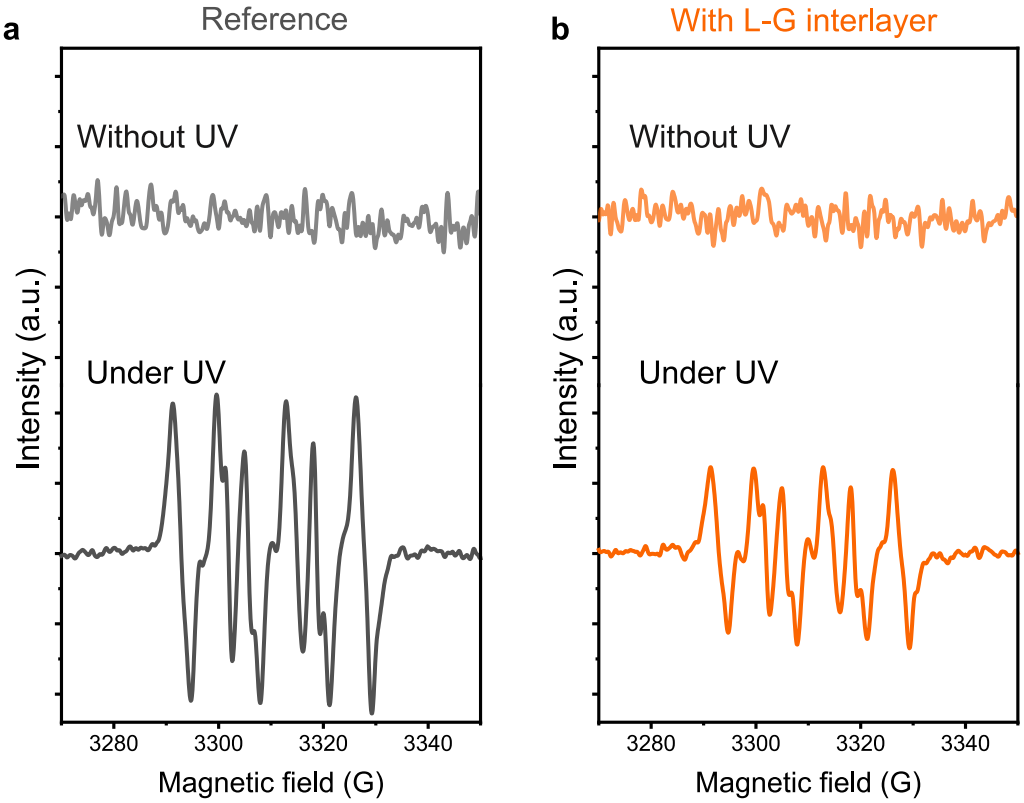

Extended Data Fig. 2 | Suppression of superoxide radical generation with the L-G interlayer. EPR spectra of the ZnO films a, without and b, with the L-G interlayer.

https://doi.org/10.1038/s41893-023-01071-2

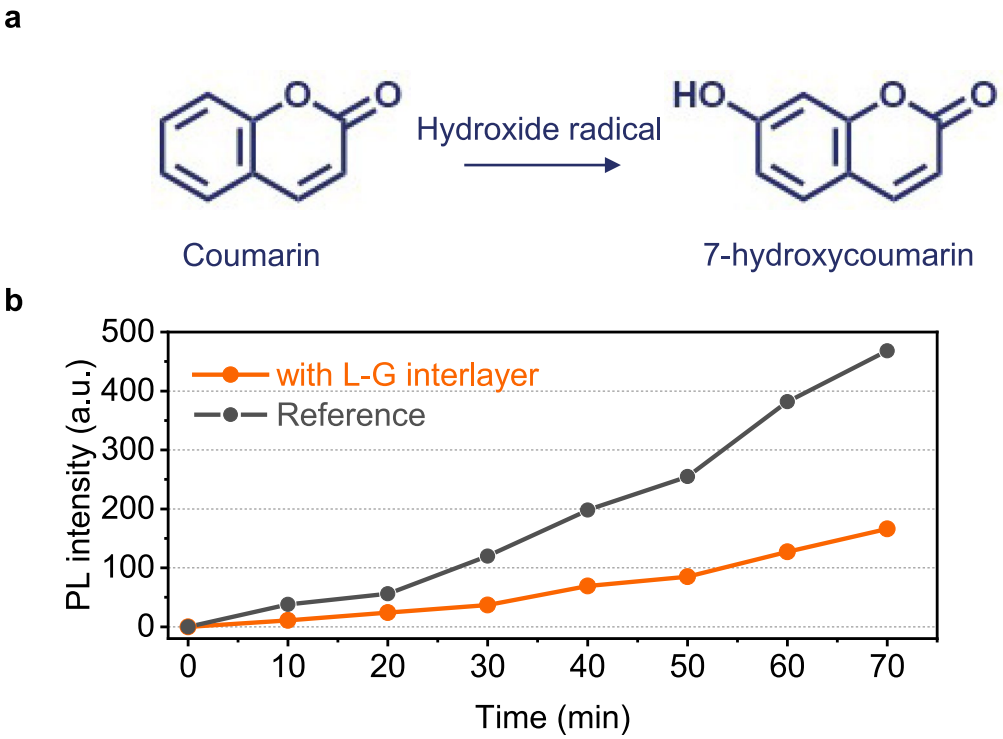

Extended Data Fig. 3 | Suppression of hydroxide radical generation with the L-G interlayer. a, Reaction that the coumarin transforms into 7-hydroxycoumarin by reacting with hydroxide radicals. b, PL intensity change at 456 nm of the solution immersed with ZnO films with and without L-G interlayer.

https://doi.org/10.1038/s41893-023-01071-2

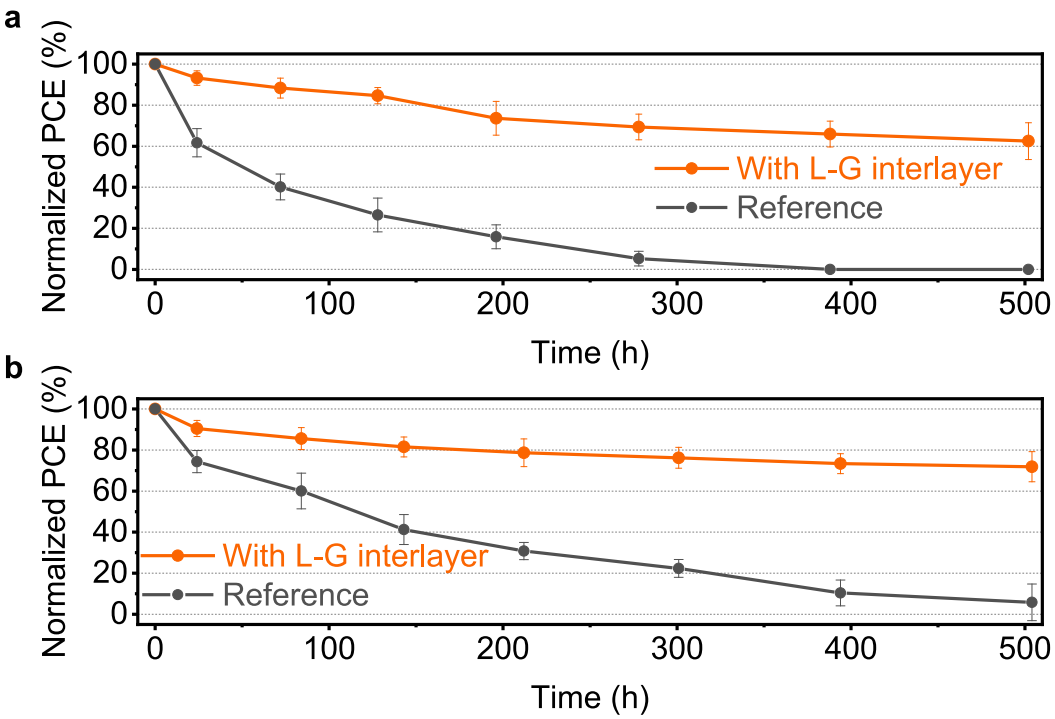

Extended Data Fig. 4 | Light and heat stability enhancements of unencapsulated devices. a, PCE changes of the devices with and without L-G interlayer during 502-hour exposure under continuous illumination. b, PCE changes of the devices with and without L-G interlayer during 502-hour heating in nitrogen glovebox.

https://doi.org/10.1038/s41893-023-01071-2

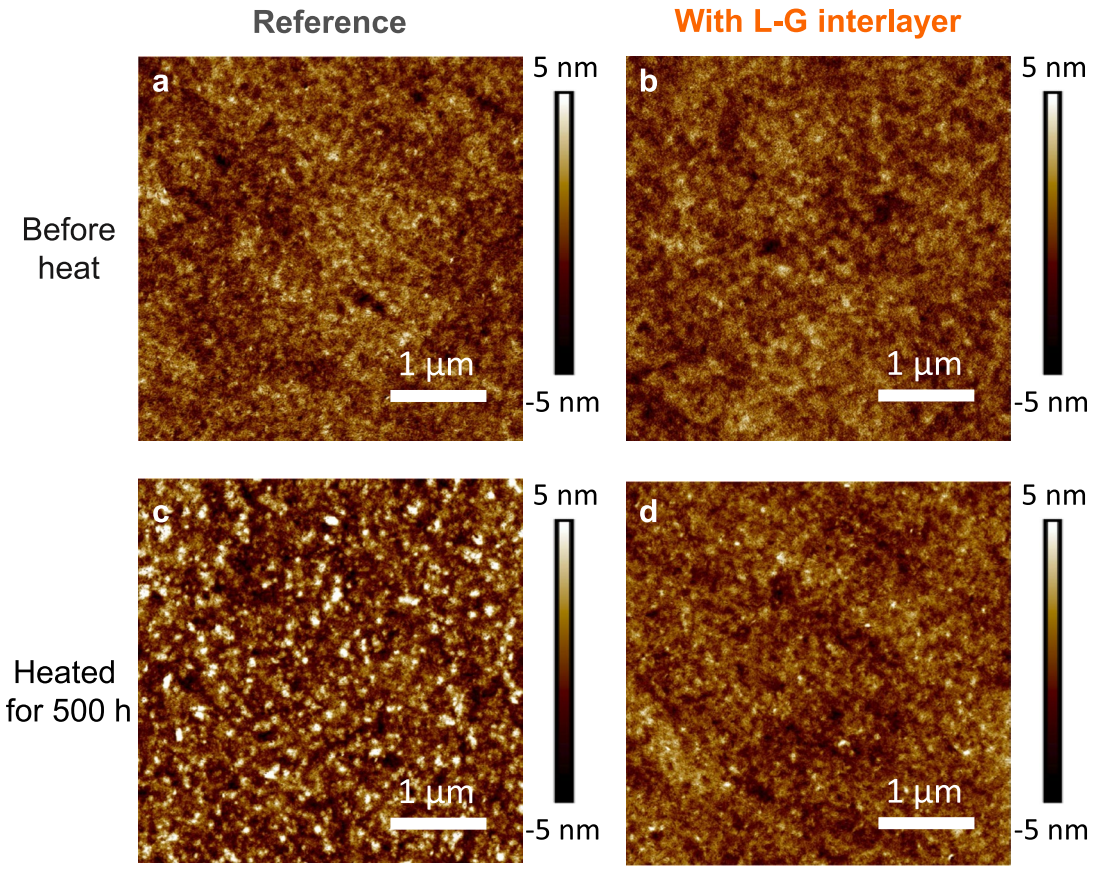

Extended Data Fig. 5 | Morphological stability of the active layers on ZnO surfaces. AFM images of the PM6/Y6 active layers on the ZnO surfaces a, c, without and b, d, with the L-G interlayer before and after heating in the nitrogen glovebox for 500 hours.

https://doi.org/10.1038/s41893-023-01071-2

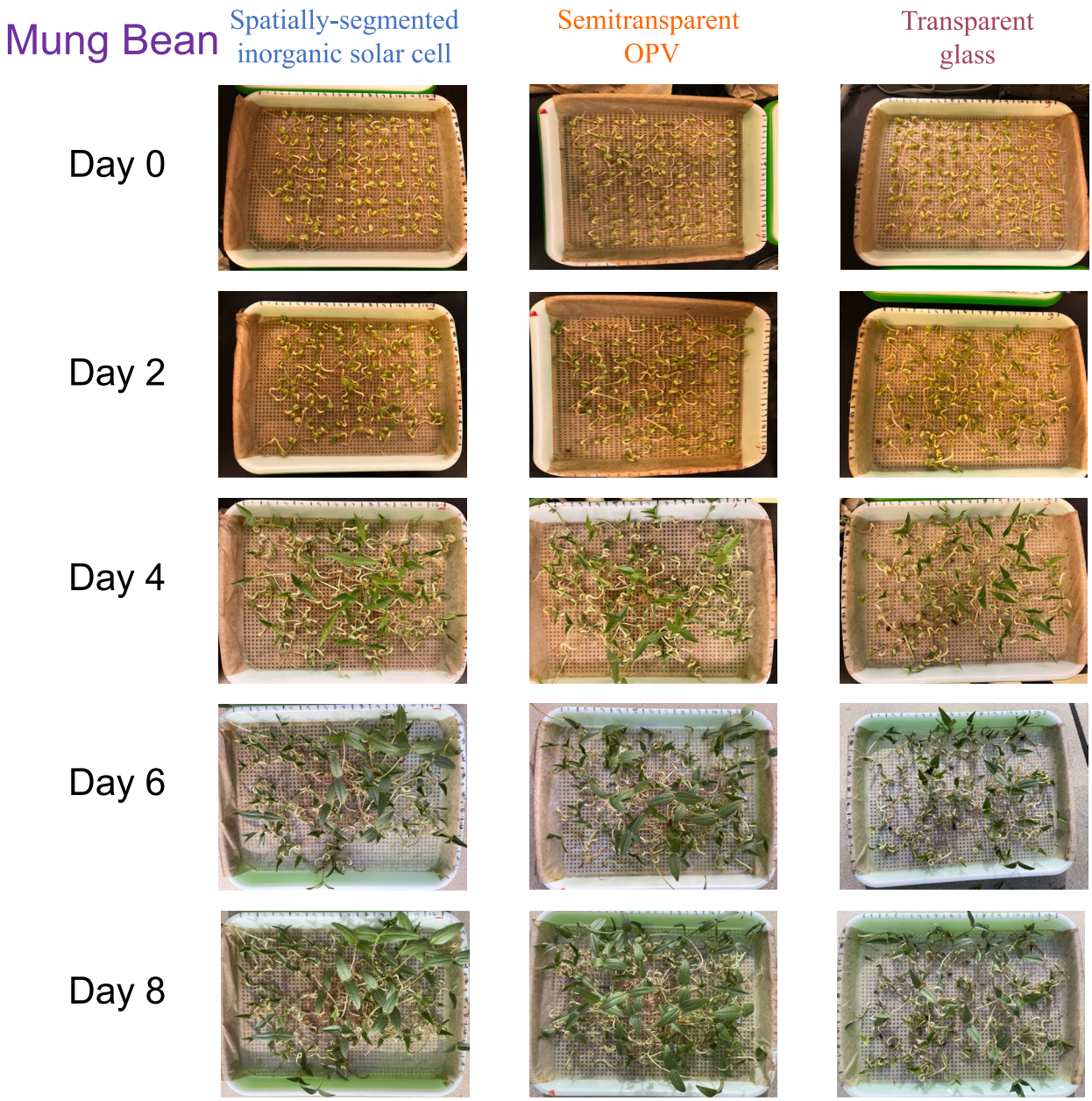

Extended Data Fig. 6 | Growth condition of the mung bean in the greenhouses. Photos that show the growth condition of the mung bean in the greenhouses with roofs of spatially segmented inorganic solar cell, semitransparent OPV, and transparent glass.

https://doi.org/10.1038/s41893-023-01071-2

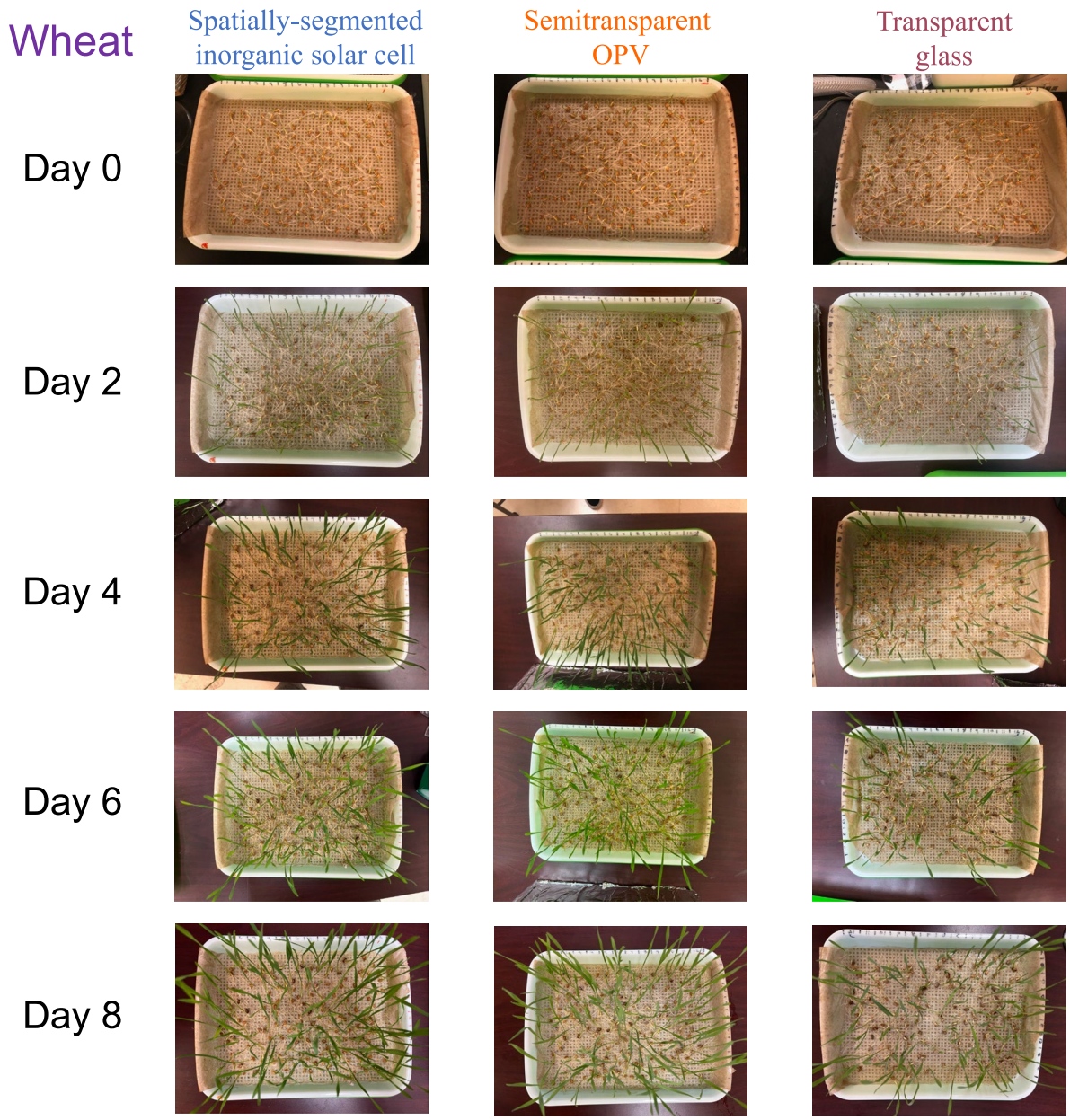

Extended Data Fig. 7 | Growth condition of the wheat in the greenhouses. Photos that show the growth condition of the wheat in the greenhouses with roofs of spatially segmented inorganic solar cell, semitransparent OPV, and transparent glass.

https://doi.org/10.1038/s41893-023-01071-2

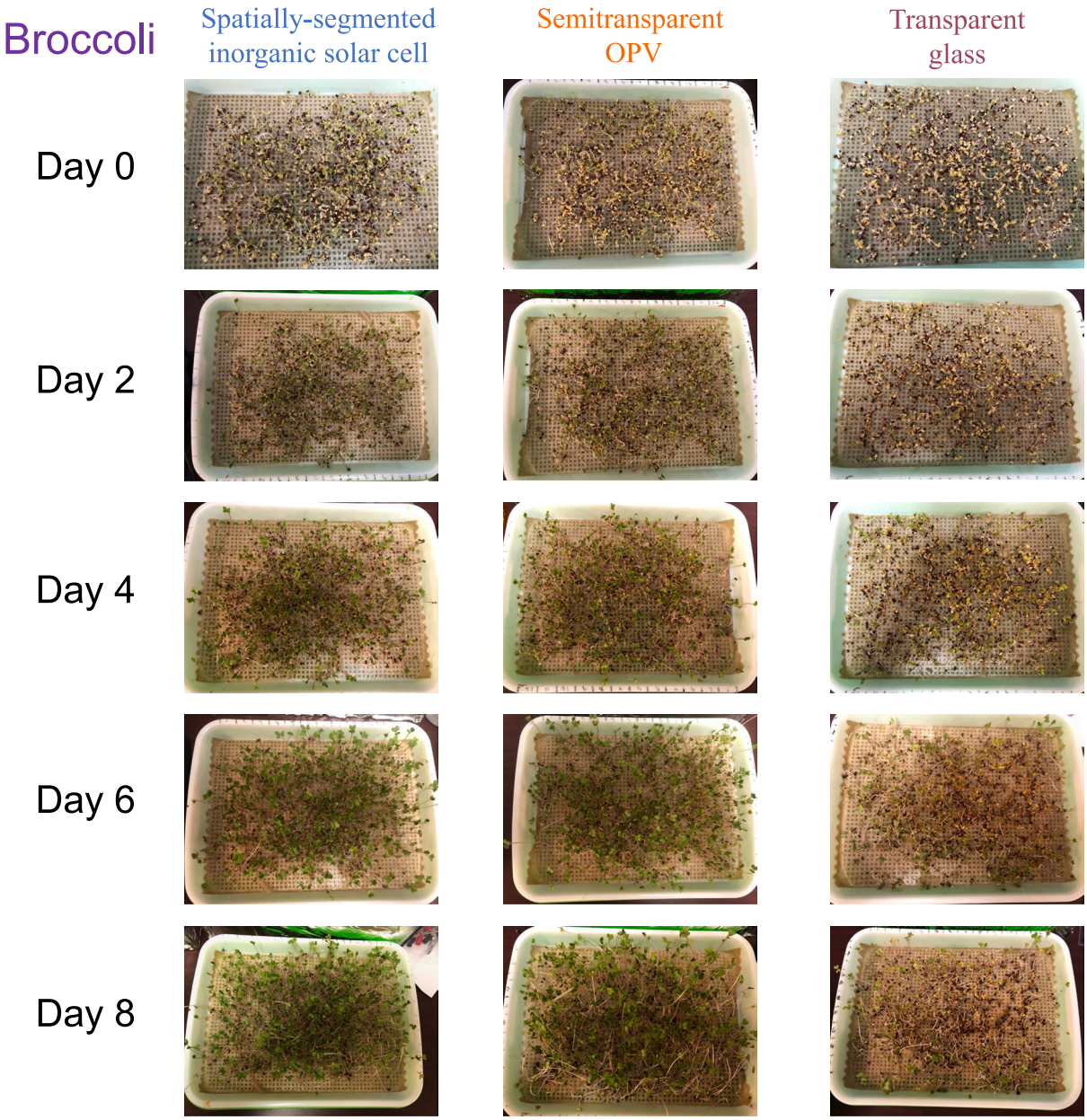

Extended Data Fig. 8 | Growth condition of the broccoli in the greenhouses. Photos that show the growth condition of the broccoli in the greenhouses with roofs of spatially segmented inorganic solar cell, semitransparent OPV, and transparent glass.